

Vertical 2D Heterostructures

Bettina V. Lotsch

Max Planck Institute for Solid State Research, 70569 Stuttgart, Germany, and Department of Chemistry, University of Munich (LMU), 81377 Munich, Germany; email: b.lotsch@fkf.mpg.de

Keynote Topic

This article is part of the 2D Materials Beyond Graphene keynote topic compilation.

Annu. Rev. Mater. Res. 2015. 45:85–109

First published online as a Review in Advance on March 30, 2015

The *Annual Review of Materials Research* is online at matsci.annualreviews.org

This article's doi:
10.1146/annurev-matsci-070214-020934

Copyright © 2015 by Annual Reviews.
All rights reserved

Keywords

2D materials, superlattices, nanosheet assembly, nanoarchitectonics

Abstract

Graphene's legacy has become an integral part of today's condensed matter science and has equipped a whole generation of scientists with an armory of concepts and techniques that open up new perspectives for the postgraphene area. In particular, the judicious combination of 2D building blocks into vertical heterostructures has recently been identified as a promising route to rationally engineer complex multilayer systems and artificial solids with intriguing properties. The present review highlights recent developments in the rapidly emerging field of 2D nanoarchitectonics from a materials chemistry perspective, with a focus on the types of heterostructures available, their assembly strategies, and their emerging properties. This overview is intended to bridge the gap between two major—yet largely disjunct—developments in 2D heterostructures, which are firmly rooted in solid-state chemistry or physics. Although the underlying types of heterostructures differ with respect to their dimensions, layer alignment, and interfacial quality, there is common ground, and future synergies between the various assembly strategies are to be expected.

1. INTRODUCTION

1.1. (R)evolution in 2D

Disruptive discoveries, shaking up the slow pace of scientific evolution now and then, are essential stepping stones that drive scientific progress toward realizing the big visions of humankind. Undoubtedly, the (re)discovery of graphene has been one such revolution, which has been radiating out from the realm of solid-state physics into all areas of condensed matter science, chemistry, and even biology over the past few years (1). Although the stunning diversity of benchmarks set by graphene's unique properties is unlikely to be found in other 2D materials, the postgraphene area is likely to hold even more promise than graphene. The reasons, put simply, are the sheer diversity of materials that can be obtained in graphene-like, monolayer form and the materials combinations that ensue from this complex basis.

1.2. NanoLego

Graphene has already produced a vast number of offspring across many classes of materials. The next big step forward in 2D research that has been embraced by the scientific community since the seminal report of two graphene monolayers sandwiching a thin boron nitride (BN) crystal (2) is the vertical stacking of individual 2D nanosheets to yield van der Waals heterostructures. As Geim & Grigorieva (1) recently pointed out, "If one considers 2D crystals to be analogous to Lego blocks. . . the construction of a huge variety of layered structures becomes possible. Conceptually, this atomic-scale Lego resembles molecular beam epitaxy but employs different 'construction' rules and a distinct set of materials." Two major visions are driving the Lego-like construction of van der Waals heterostructures with judiciously designed layer sequences: (a) the ability to precisely engineer heterostructures revealing entirely new physical phenomena and (b) the design of tailor-made, artificial bulk solids that cannot be accessed by classical high-temperature solid-state chemistry (3). Although these two visions represent two sides of the same coin, the former is firmly rooted in physics, whereas the latter reflects a rather chemical perspective. Their common ground, however, is the ability to sculpture and create new materials at will and with an unprecedented level of control from the smallest building blocks one can imagine: 2D nanosheets.

1.3. Materials Matter

If one looks at the materials basis, the materials choice for next-generation 2D materials and their heterostructures is restricted by the required anisotropic nature of the respective bulk materials, i.e., strong covalent bonding within the layers held together by weak interlayer interactions. Isolating individual layers from the parent bulk crystal with minimal structural disruption and a low number of defects is so far possible only via mechanical delamination from layered van der Waals solids featuring very weak dispersive interactions between the layers ($\sim 40\text{--}70$ meV) (4), as schematically outlined in **Figure 1a**. The bottleneck of exclusively relying on van der Waals solids can be ameliorated by considering another class of layered materials, namely ionic layered materials (**Figure 1b**). These materials offer alternative anisotropic bonding modes, whereby strong intralayer bonding alternates with medium-strong electrostatic interlayer bonding mediated by molecular or extended ionic species acting as a glue to keep the layers together.

At the opposite end of the spectrum, isotropic 3D solids are not amenable to either micromechanical cleavage or chemical exfoliation, which consequently removes these types of materials from the 2D portfolio. There are, however, ways of scaling 3D solids down into atomically

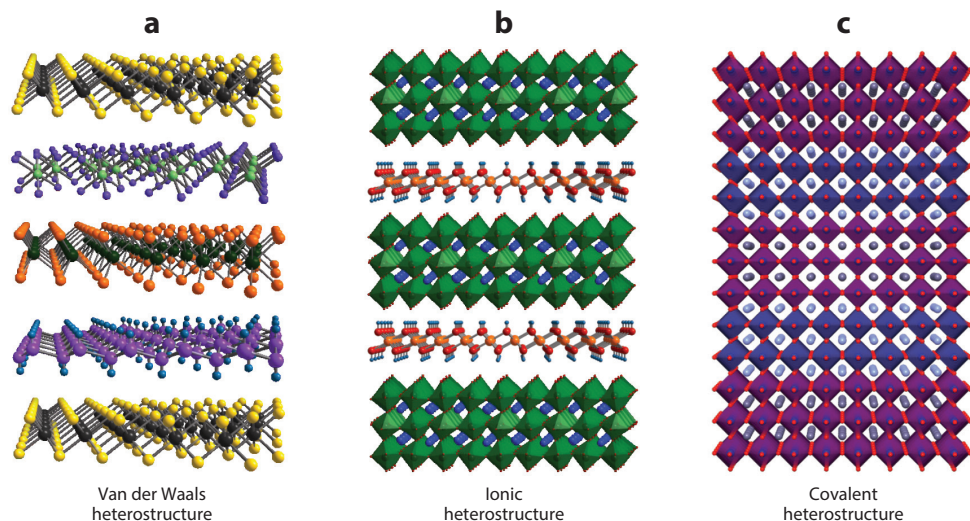


Figure 1

Schematic illustrations of three prototypical types of heterostructures, which are classified on the basis of the type and strength of bonding between their building blocks: (a) van der Waals; (b) ionically bonded; and (c) epitaxially grown, covalently bonded heterostructures.

thin layers that are effectively their 2D counterparts. The technical progress and refinement of advanced molecular beam epitaxy (MBE) and pulsed laser deposition and related deposition techniques have been at the heart of the ability to engineer epitaxially grown oxide superlattices with atomically clean interfaces and a judicious choice of layer sequences with sub-unit-cell precision (5). Nevertheless, such epitaxially grown heterostructures are typically derived from 3D solids—the vast majority being 3D perovskite and spinel based—which cannot be isolated in atomically thin form due to the large number of dangling bonds and, hence, increased reactivity and propensity for surface reconstruction (**Figure 1c**). Likewise, nanolaminates composed of different types of 3D dielectrics such as ZnO, TiO₂, Ta₂O₅, or Al₂O₃, deposited by atomic layer deposition into multilayers a few nanometers across (6), are not part of this review. Here, we limit our discussion to 2D heterostructures that can be, in principle, deconstructed into their individual building blocks, i.e., nanosheets, which can be isolated with minimal structural changes and handled individually.

Below, we discuss the different classes of artificial heterostructures, with a focus on the top-down and bottom-up assembly methods at hand. Finally, we take a glimpse at the extremely diverse set of properties inherent in and the potential applications for this diverse new class of nanostructured materials.

2. TYPES OF HETEROSTRUCTURES AND CLASSIFICATION

With the ability to sculpture artificial heterostructures by physical and chemical means, the existence of a wide variety of bulk—sometimes naturally occurring—heterostructures has often been overlooked. Textbooks on solid-state chemistry abound with intergrowth structures, all of which feature two or more distinct layer types and, hence, planar compositional heterogeneity. Examples of such natural and artificial bulk heterostructures include aluminosilicates of the phyllosilicate family such as the mineral chlorite (Mg₅Al)(Si₃Al)O₁₀(OH)₈, where cationically charged Brucite-type Mg₂Al(OH)₆⁺ layers reside between anionically charged Mg₃AlSi₃O₁₀(OH)₂⁻ layers; misfit

layer chalcogenides, prominently represented by compounds of type $[\text{MX}]_{1+x}[\text{TX}_2]_m$ ($M = \text{Sn, Pb, Sb, Bi}$, rare earth; $T = \text{Ti, V, Cr, Nb, Ta}$; $X = \text{S, Se}$; $0.08 < x < 0.28$; $m = 1, 2, 3$) (7); and the family of Aurivillius-type layered perovskites with composition $[\text{Bi}_2\text{O}_2][\text{A}_{n-1}\text{B}_n\text{O}_{3n+1}]$, for example, the piezoelectric compound $\text{Bi}_4\text{Ti}_3\text{O}_{10}$. These materials can be grown by conventional solid-state chemical methods, and although some of them show incommensurability or turbostratic disorder (8), their intricate structures are well characterized, providing us with the crystallographic tools that will be needed to understand more complex artificial heterostructures assembled from the bottom up, once they are made.

Compared with the large number of natural heterostructures at hand, the range of artificial heterostructures appears to be rather limited, if not tiny—and yet, there is a great diversity waiting to be unraveled. As mentioned above, three types of artificially assembled heterostructures can be distinguished: (a) van der Waals heterostructures, (b) electrostatically assembled heterostructures, and (c) epitaxially grown 3D heterostructures. In the following, we limit our discussion to types *a* and *b*, drawing the demarcation line between heterostructures based on individual nanosheets (types *a* and *b*) and those derived from epitaxially intergrown 3D solids (type *c*).

3. FABRICATION OF 2D HETEROSTRUCTURES

The range of layered bulk solids that have been exfoliated down to the few- or monolayer level has been rapidly increasing over the past few years. The quest for dimensionally reduced graphene analogs has reached almost all corners of the periodic table, and the available toolbox of nanosheet materials can be pragmatically (rather than systematically) classified into the following categories: graphene, chalcogenides, oxides and hydroxides, group IV semiconductors and Zintl phases (9, 10), ceramics and nitrides (11–13), and soft 2D materials such as polymers and coordination networks (14, 15). For a comprehensive treatment of the 2D building blocks that are available for the assembly of heterostructures, the reader is referred to recent reviews on the topic as well as related reviews within this volume (4, 16–20).

In the following, we summarize existing protocols for creating van der Waals heterostructures by mechanical top-down and direct-growth bottom-up approaches. We then proceed to review the synthesis of electrostatically assembled heterostructures by chemical solution processing.

3.1. Van der Waals Heterostructures: Mechanical Transfer Methods

The most straightforward fabrication of vertical van der Waals heterostructures is by a stepwise mechanical transfer of arbitrary 2D layers onto a substrate, i.e., by the top-down manipulation of individual nanosheets one by one. A number of techniques have been developed to address the challenge of transferring as-made large-area graphene from its growth substrate or a postexfoliation support to arbitrary substrates with high fidelity. These transfer methods can, in principle, be used for the bottom-up fabrication of high-quality van der Waals heterostructures with multiple layers as well. The transfer methods that have been developed—carrier foil transfer and stamping—are variations of the following basic schemes and depend on whether the initial 2D layer needs to be transferred from the growth substrate or can be mechanically exfoliated directly on top of the transfer polymer. In the carrier foil method, the 2D material is covered by or exfoliated onto a poly(methyl methacrylate) (PMMA) film or a thermal release tape [e.g., Nitto Denko's REVALPHA thermal release (21)] and is transferred to the target substrate. The 2D material is released either by dissolving the PMMA or by heating the tape (**Figure 2**). Variations of this theme abound, making use of additional sacrificial layers and different types or thicknesses of the transfer polymer. Ideally, the 2D material is exfoliated onto a PMMA film that is deposited on another

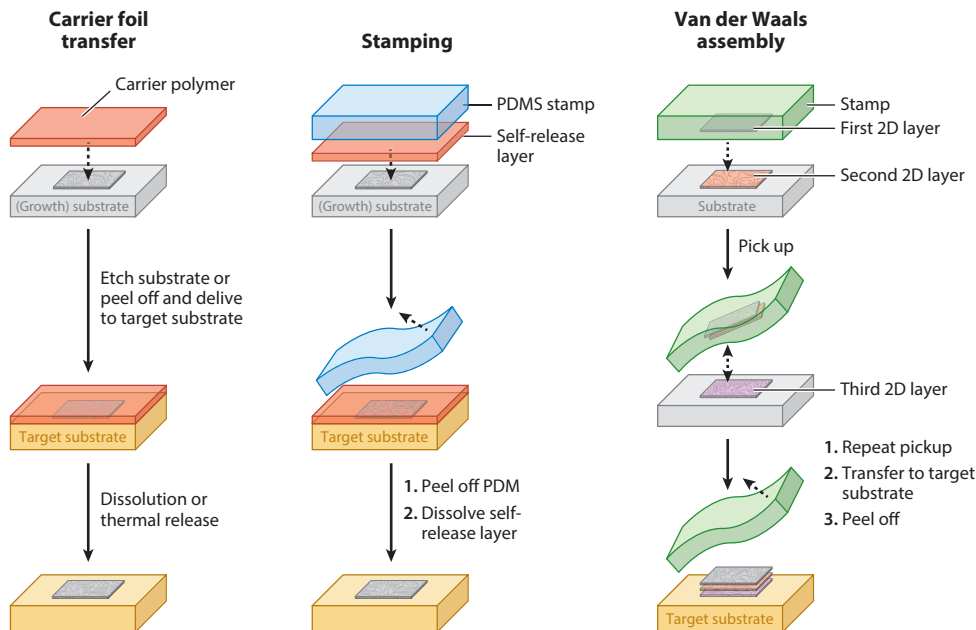


Figure 2

Schematic illustration of different transfer methods relying on various types of polymer film and elastomer combinations for the mechanical transfer of nanosheets and dry assembly of van der Waals heterostructures. Abbreviation: PDMS, polydimethylsiloxane.

sacrificial, water-soluble polymer layer, such as poly(vinyl alcohol), placed on a Si/SiO₂ substrate. The three-layer structure is then immersed in a water bath, where the water-soluble layer is dissolved, releasing the 2D layer/PMMA film, which then floats at the air/water interface (22).

Release of the 2D layer/polymer film from the substrate can also be facilitated by making use of the capillary forces between a hydrophobic polymer (e.g., cellulose acetate butyrate) and a hydrophilic substrate, leading to a dynamic liftoff of the 2D layer/polymer film when a drop of water is placed at the hydrophilic/hydrophobic interface (the so-called wedging method) (23).

Despite its versatility, a major drawback of this method for multilayer assembly is the limited ability to precisely align the layer to be transferred with the target layer due to the lack of mechanical stability of the thin polymer film. This limitation can in part be overcome by attaching the backside of the polymer to a robust and transparent substrate. Nevertheless, the involvement of solvents (some of them aggressive, such as KOH) in the removal of the transfer polymer and annealing steps at temperatures of approximately 100°C, or both, limit the use of this transfer method for delicate 2D materials. Another limiting factor is the interfacial quality of the 2D layers, which have been in contact with different types of polymers and solvents throughout the process and often suffer from incomplete removal of the sacrificial polymer layers.

Microcontact stamping using polydimethylsiloxane (PDMS) or other elastomer stamps is the second general strategy to transfer 2D materials from one substrate to another. In principle, this process is rather straightforward and does not require elaborate chemical dissolution or thermal detachment steps, hence lending itself well for the successive dry transfer of multiple 2D layers on a substrate. In addition, this method also has a built-in alignment capability by taking advantage of the transparency of the stamp and its mechanical robustness and by allowing for the use of

prepatterned stamps and, hence, the fabrication of patterned heterostructures. Although no capillary forces are involved in this method for detachment purposes and hence freely suspended structures that might otherwise collapse are accessible, the method requires a delicate balance of surface and adhesion properties between the stamp and the 2D layer on the one hand, and the 2D layer and the target substrate on the other hand. In practice, the level of interfacial quality strongly depends on the quality of the stamp and on the completeness of the transfer.

A number of variations of the dry stamping method have been devised to stamp 2D layers onto arbitrary surfaces, including soft and holey substrates, with minimum contamination of the exposed interfaces. One such variation is the use of sacrificial polymer layers that act both as protection of the 2D layer to be transferred and as a means of facilitating the transfer process to the acceptor substrate by adjusting the adhesive forces at the different interfaces. Li et al. (24) and Song et al. (25) developed transfer methods relying on a thin self-release or carrier polymer layer—poly-L-lactic acid, polystyrene, or other hydrophobic aromatic hydrocarbon or fluorocarbon polymers—sandwiched between the 2D material to be transferred and a conventional PDMS elastomer stamp (**Figure 2**). The PDMS/polymer/2D layer sandwich can be removed from the Si/SiO₂ substrate by means of capillary forces exerted by a water droplet penetrating between the hydrophilic Si/SiO₂ substrate and the hydrophobic polymer interface (24). The peeled-off film is then brought into conformal contact with the acceptor surface, and the PDMS stamp is removed by a 50°C bake, whereas the carrier polymer is washed away with dichloromethane.

As the removal of either the stamp or the sacrificial polymer layer may not be complete and may leave behind microscopic impurities on the exposed surface of the 2D material, the development of a completely stamp- and polymer-free transfer method appears to be the next crucial step. In fact, Dean and coworkers (26) presented a so-called van der Waals assembly scheme, which circumvents the need to use sacrificial layers in contact with the 2D components in a stack, except for the topmost layer (**Figure 2**). A van der Waals crystal (or simply an exfoliated monolayer) is placed on top of a carrier polymer [e.g., 1- μ m layer of polypropylene carbonate (PPC) on a Si wafer], and the PPC/2D layer is then placed on top of a transparent PDMS stamp. Subsequently, the sandwich structure is brought in contact with another 2D crystal exfoliated onto a Si/SiO₂ wafer, which is heated at 40°C. As shown in **Figure 3**, this process can be repeated several times, provided that the van der Waals adhesive force to the 2D stack built up on the PPC layer is stronger than the adhesion to the substrate. The PPC can be washed away by chloroform, leaving behind the clean multilayer stack. The beauty of this method lies in the fact that the critical interfaces within the stack are not in contact with a polymer throughout the entire transfer process, thus reducing the contamination risk and trapping of defects at the interfaces.

The mechanical transfer method generally leads to turbostratically disordered stacks without lateral layer registry unless the layer alignment is meticulously controlled by means of a micromanipulator (27). Determination of the layer misalignment angle is rather straightforward, even for stacks with more than two layers, by means of analyzing the Moiré patterns in STM, conductive AFM, or HRTEM images or by deconvoluting the electron diffraction patterns of heteromultilayers (**Figure 4**) (28).

Although the mechanical transfer of 2D layers has been explored for various layer combinations and substrates (22), the reported heterostructures are typically limited to two to four monolayers, with some notable exceptions (see **Figure 5**) (29), which is a testament to the complex multistep procedures involved in the mechanical transfer. In contrast, the interfacial quality is exceptionally high in many cases, giving rise to multilayer structures with atomically clean interfaces, which are critical for many device applications (25). Gorbachev and coworkers (29) studied the interfacial structure of multilayer graphene (MLG)/h-BN (hexagonal BN) superlattices by cross-sectional TEM and locally resolved EELS. They found that ubiquitous hydrocarbon contaminations

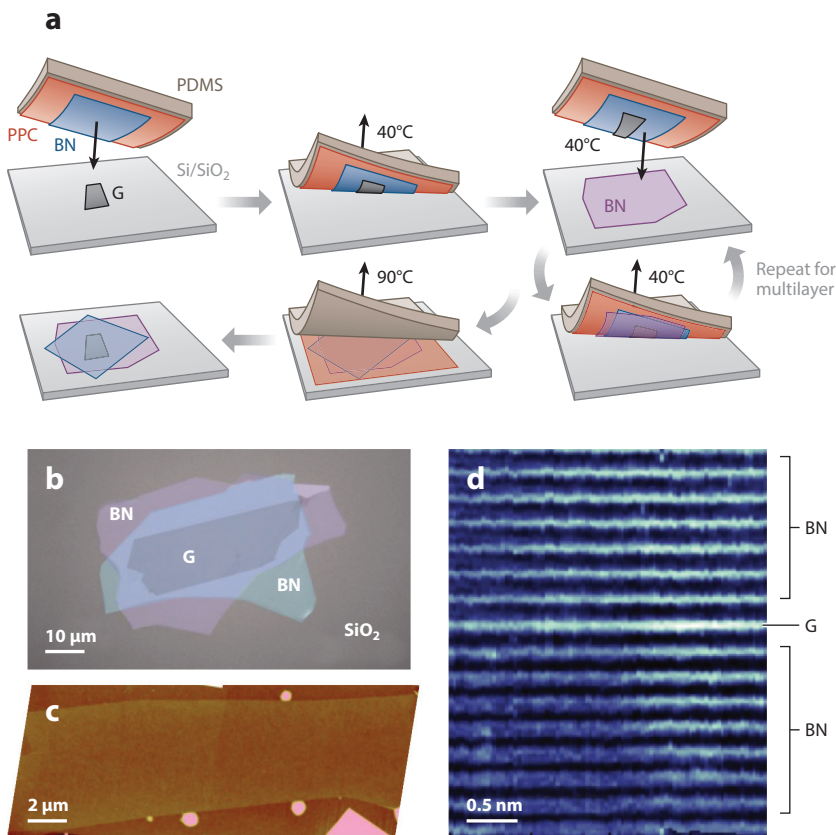


Figure 3

(a) Schematic of the polymer-free van der Waals assembly process. (b) Optical image of a h-BN/G/h-BN heterostructure assembled according to panel a. (c,d) AFM (c) and high-resolution cross-sectional ADF-STEM (d) images of the multilayer structure, showing wrinkle-free and atomically clean interfaces. Abbreviations: G, graphene; h-BN, hexagonal boron nitride; PDMS, polydimethylsiloxane; PPC, polypropylene carbonate. Adapted with permission from Reference 26.

adsorbed on the 2D crystals during the fabrication steps tend to diffuse over micrometer-scale distances within the stack, segregating into isolated pockets and thus leaving the 2D interfaces largely atomically clean. Importantly, the interlayer separation of the h-BN and graphene planes is indistinguishable from the basal plane distance in bulk h-BN, which confirms that significant contamination of the interfaces is unlikely (29).

3.2. Direct Growth of 2D Heterostructures

The mechanical transfer method described in Section 3.1 is fairly limited with respect to the automated fabrication of large-scale heterostructures with multiple layers and upscaling. Therefore, alternative paths toward van der Waals heterostructures, such as their direct bottom-up growth from appropriate precursors by using vapor-phase deposition techniques, have been recently emerging. Such protocols hold promise with respect to future device integration and automation, although the rational control of the growth process is still a great challenge.

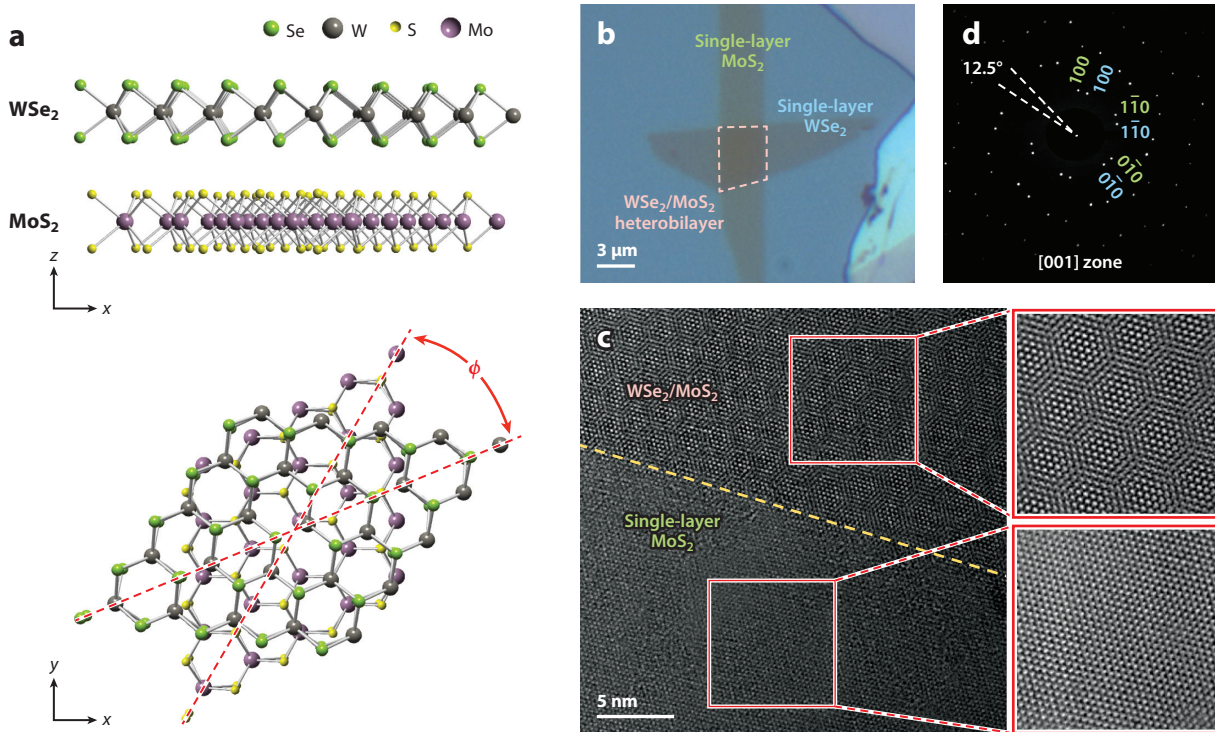


Figure 4

(a) Structure of a WSe_2/MoS_2 bilayer viewed along the y -axis (top) and z -axis (bottom); ϕ is the misalignment angle. (b) Optical microscope image of the WSe_2/MoS_2 bilayer on Si/SiO₂. (c) HRTEM image of the boundary region between single-layer MoS_2 and the WSe_2/MoS_2 bilayer with the resulting Moiré pattern (top right). (d) Selected-area electron diffraction pattern of the heterostructure along [001]. WSe_2 and MoS_2 are indexed in blue and green, respectively, and $\phi = 12.5^\circ$. Adapted with permission from Reference 28.

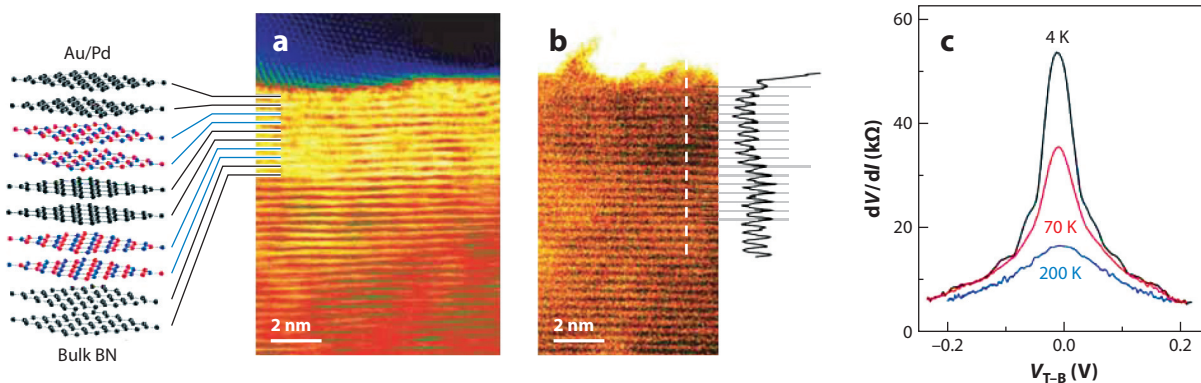


Figure 5

(a) Schematic layer sequence and corresponding bright-field cross-sectional STEM of a stack comprising graphene and hexagonal boron nitride bilayers. (b) HAADF-STEM image of the same heterostructure. The intensity line profile (length 7 nm, integration width 5 nm) is shown to the right. (c) Vertical transport properties represented by the differential resistance dV/dI as a function of bias voltage, V_{T-B} , applied between the top and bottom graphene bilayers. dV/dI exhibits a zero-bias peak that grows with decreasing temperature. Adapted with permission from Reference 29.

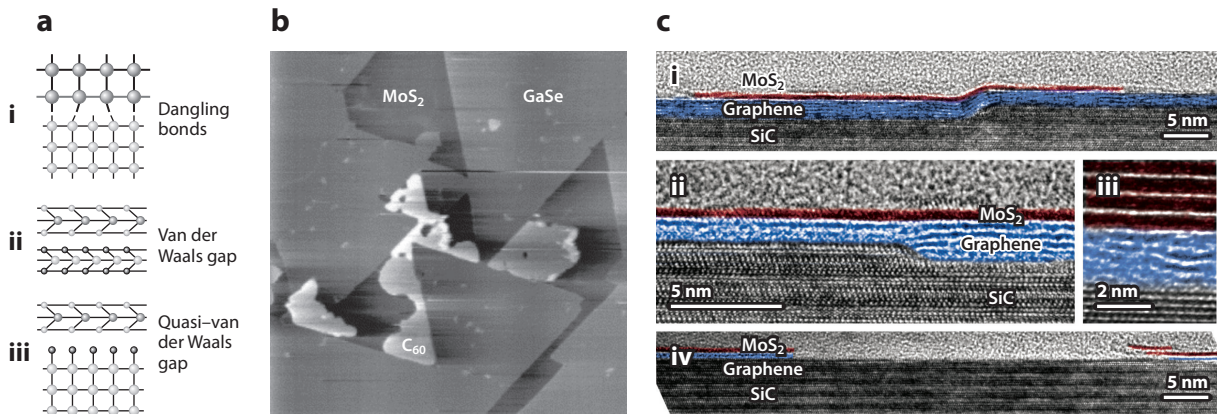


Figure 6

(a) Schematic illustration of different interface terminations defining the heteroepitaxial growth mode and lattice matching conditions: (i) dangling bonds, (ii) van der Waals gap, and (iii) quasi-van der Waals gap enabling 2D growth on passivated surfaces of 3D materials. (b) AFM image ($1.2 \mu\text{m} \times 1.2 \mu\text{m}$) of a C_{60} film on submonolayer GaSe grown epitaxially on a MoS_2 substrate. The C_{60} film (*bright parts*) grows only on uncovered MoS_2 regions (*dark parts*). (c) Cross-sectional HRTEM images of monolayer MoS_2 grown on quasi-free-standing epitaxial graphene/SiC by CVD. MoS_2 is shaded in dark red, and graphene is shaded in blue. (i,ii) Nucleation occurs at the $(1\bar{1}0n)$ step edges and extends onto the (0001) terrace regions, irrespective of the graphene topology below. (iii) Defective graphene initiates the growth of multilayer MoS_2 . (iv) In contrast, nucleation and growth of MoS_2 are promoted by graphene, rather than by bare SiC. Panels *a* and *b* adapted with permission from Reference 32; panel *c* adapted with permission from Reference 47.

3.2.1. Van der Waals epitaxy. Van der Waals epitaxy (VDWE) refers to the oriented in situ growth of 2D layers by vapor-phase deposition, giving rise to homo- or heterojunctions that are held together by weak van der Waals forces. In fact, VDWE was described in 1984 for the first time by Koma and colleagues, who demonstrated the heteroepitaxial growth of NbSe_2 on a cleaved 2H- MoS_2 single crystal by MBE, in spite of a lattice mismatch as large as 10% (30–32). The defining feature of VDWE is the weak interaction across the 2D heterojunction and the absence of dangling bonds at the atomically abrupt and defect-free interface (**Figure 6**). The weak interfacial van der Waals forces result in a drastically relaxed lattice matching condition, allowing for the fabrication of a variety of heterostructures based on 2D systems, including those that are highly lattice mismatched (more than 50%) (32), as well as on hybrid 2D/3D systems, given that the latter are appropriately terminated (**Figure 6a**).

Significant progress in the deposition of large-scale, single-crystalline monolayers has been made by employing a wide range of catalytic and noncatalytic solid-vapor processes. To enable the direct growth of multilayer heterostructures, one key requirement is the ability to grow different types of 2D materials in unilamellar form on arbitrary substrates. Therefore, (a) compatibility of the substrate and the underlying heterostack with the process conditions has to be ensured, (b) the growth process should be largely independent of the substrate, and hence (c) noncatalytic growth processes are needed. In recent years, processes enabling the noncatalytic growth of various 2D materials on insulating surfaces such as MgO (33), ZnS, mica (34), Si/SiO₂, and sapphire have been developed. Such processes include the heteroepitaxial growth of large-scale graphene on h-BN by low-pressure, high-temperature CVD (35) or a plasma-enhanced CVD process. By breaking down methane through a remote plasma source, the need for a catalytically active metal source can be eliminated, and graphene growth is possible at moderate temperatures of 500°C (36). Importantly, these studies show that graphene can be precisely aligned with the underlying h-BN

lattices by VDWE, giving rise to commensurate h-BN/graphene heterostructures with minimal lattice mismatch, well-defined orientation, and a lattice misalignment of less than 0.05° (35).

Apart from the successful growth of graphene on h-BN, a range of transition metal dichalcogenides (TMDs) have been grown on various substrates, yet the controlled growth of large-scale or even wafer-size monolayer TMDs with few grain boundaries and adlayers currently remains a major challenge (37). One reason is the suppressed nucleation of adatoms on the surface of a 2D material owing to its very small surface energy (38). Typical procedures used for the direct growth of TMDs by vapor-phase processes are the sulfurization (or selenization) of ultrathin metal or metal oxide films (39, 40), thermolysis of metal-sulfur-containing precursors (16–18), the vapor-phase reaction of transition metal oxides with chalcogen precursors (34, 41, 42), and physical vapor transport of MoS_2 (43). Restricting the growth process to the surface is a key requirement to realize atomic-layer control of TMD growth, and CVD-based processes have recently been optimized toward controlling both the surface/substrate interactions and the nucleation and growth process to achieve epitaxially grown TMDs on other single-crystalline 2D surfaces (44–46). Epitaxial growth of MoS_2 on graphene was demonstrated by Kong and coworkers (44), who deposited MoS_2 flakes onto CVD-grown, Cu foil-supported graphene by employing a low-pressure CVD process using $(\text{NH}_4)_2\text{MoS}_4$ dissolved in dimethylformamide (DMF) as the precursor. These researchers observed that the growth template has a major impact on the quality and growth mode of the TMD layer deposited from the vapor phase and that step edges, wrinkles, and defects act as nucleation sites (44). Lin et al. (47) reported the growth of MoS_2 , WSe_2 , and h-BN on different types of graphene epitaxially grown on SiC(0001) and found that the growth morphology is strongly influenced by the structural quality, coupling to the SiC substrate and hence to buildup of strain in the underlying graphene growth template (**Figure 6c**). The important role of the surface/epilayer interactions in the growth process was demonstrated for the growth of MoS_2 on surfaces primed with graphene-like seeding layers, including reduced graphene oxide and various aromatic hydrocarbon molecules. After drop casting hydrophilic perylene-3,4,9,10-tetracarboxylic acid tetrapotassium salt (PTAS) or other molecular promoters on various surfaces such as amorphous SiO_2 , the growth of rather uniform monolayer and multilayer MoS_2 with large lateral sizes and high crystallinity was observed (41, 42, 48). Apparently, molecular aggregates of the aromatic molecules initiate and promote the layer growth of TMDs. To achieve large-scale TMD monolayers, nucleation must be the rate-controlling step in the seed-initiated growth, whereas 2D layer growth should be favored in the initial growth stage (41, 42). With PTAS as the seeding layer, MoS_2 and WS_2 monolayers with high tolerance to substrate quality and corrugations were fabricated in a scalable ambient-pressure CVD process by using MoO_3 or WO_3 and sulfur as precursors (42), resulting in TMDs with electronic and optical quality comparable to that of exfoliated TMDs.

In general, controlling the growth mode in vapor-phase epitaxial processes requires insights into the chemical potential of the first adsorbed layers and, hence, consideration of the adsorbate (γ_{ads}) and substrate (γ_{sub}) free energies, the interface free energy (γ_{inter}), and strain buildup at the substrate/adsorbate interface. To implement strict 2D growth, the growth process should be dominated by strong surface adhesive forces between the substrate and the nucleating adsorbate material, favoring a Frank–van der Merwe (FM) mechanism [i.e., 2D layer-by-layer growth, where $\gamma_{\text{ads}} + \gamma_{\text{inter}} < \gamma_{\text{sub}}$], rather than Volmer–Weber (VW) growth that results in island formation. In practice, VW or Stranski–Krastanov (SK) growth (layer plus island formation) is often observed in VDWE, in which the sum of the surface free energy of the growth material and the interface free energy is larger than or approximately the same as the substrate free energy, $\gamma_{\text{ads}} + \gamma_{\text{inter}} \geq \gamma_{\text{sub}}$ (49). Therefore, measures have to be taken to enhance the surface adhesive force over the cohesive forces within the adlayers. According to Saidi (45), the growth of TMDs on undoped graphene substrates generally follows a VW-type growth process, resulting in thick TMD

films. However, by nitrogen doping of graphene or employing graphene with Stone-Wales defects, the TMD/graphene adhesive energy is increased, thus transforming the growth mechanism into a FM-like or SK-like growth mode, which favors the 2D growth of ultrathin TMD layers (45).

3.2.2. Van der Waals heterostructures by reactive annealing. Johnson and coworkers (50) have developed an intriguing synthetic method capable of producing complex van der Waals superlattices via the deposition of elemental sources and subsequent annealing. The procedure, referred to as the modulated elemental reactant technique, allows for the rational and highly modular design of compositionally complex superlattices based on layered compounds. This design strategy has been used to construct a large series of mixed chalcogenide superlattices of the $[MX_2]_m[M'X_2]_n$ type, such as $[\text{NbSe}_2]_6[\text{TiSe}_2]_6$ (50), and artificial intergrowth compounds $[(MX)_z]_m[(T_xT'_{1-x})X_2]_n$ similar to the layer misfit chalcogenides, such as $[(\text{SnSe})_{1.16-1.09}]_1[(\text{Nb}_x\text{Mo}_{1-x})\text{Se}_2]_1$ (8). The heart of this concept is the deposition of amorphous precursors, which are compositionally modulated in space so as to mimic the elemental distribution in the desired heterostructured product and to minimize diffusion lengths. Controlled interfacial nucleation is then induced by mild thermal annealing, which results in the formation of kinetically trapped, metastable layered heterostructures with a custom-made layer sequence (Figure 7). A characteristic feature of this growth technique is that, although crystal growth proceeds in the in-plane direction, it does not have a built-in control on the layer alignment out of plane, hence resulting in so-called ferecrystals with significant turbostratic disorder along the layer stacking direction. Because this process is not epitaxial, the modulated elemental reactant technique is more widely applicable to compounds with greatly

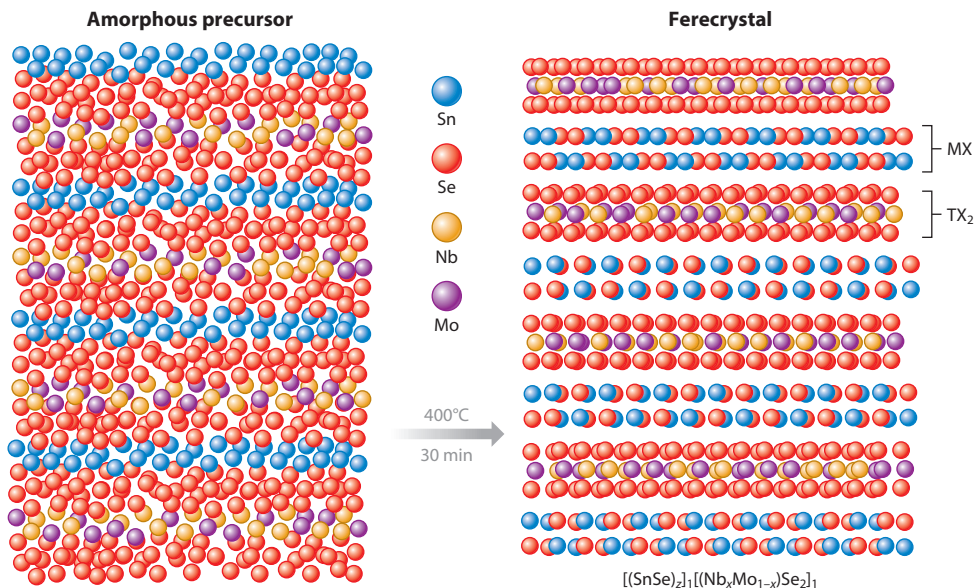


Figure 7

Synthesis scheme for the formation of artificial chalcogenide intergrowth compounds based on the modulated elemental reactant technique. An elementally modulated amorphous precursor deposited by PVD is transformed into metastable, rotationally disordered layered chalcogenide superlattices by mild annealing. Adapted with permission from Reference 8.

dissimilar chemistries and crystal structures and to materials that would require prohibitively high growth temperatures in MBE, such as carbides (50).

3.3. Electrostatically Assembled Heterostructures

The bottom-up low-temperature assembly of charged nanosheets into artificial heterostructures has been actively pursued since the 1990s by drawing on well-established concepts of colloidal chemistry and *Chimie Douce* (51, 52). A major asset has been the rational design of complex materials by deconstruction of solids into their basic structural building units and reconstruction into heterostructures, very much akin to the concept of total synthesis ubiquitous in organic synthetic chemistry (53). The low-temperature design of artificial and metastable solids that are inaccessible by thermodynamically driven, high-temperature solid-state synthesis was christened “molecular beaker epitaxy” by Mallouk and colleagues (51) in the 1990s, implying that it can be viewed as the solution-based counterpart of gas-phase MBE. Sasaki and others extended this methodology to all-inorganic heterostructures by combining oxidic anionic and cationic nanosheets by electrostatically driven self-assembly (54–58).

In contrast to van der Waals solids, ionically bonded layered materials are less amenable to mechanical cleavage and are typically exfoliated by means of solution processing, i.e., through ion-exchange intercalation, followed by liquid-phase exfoliation. A widely established protocol for the efficient delamination of many ionic layered oxides, including perovskites and titanates, into individual nanosheets is by protonation of the alkali-containing precursors, followed by cation exchange with the bulky tetrabutylammonium hydroxide, where neutralization of the protons by the tetrabutylammonium counterion OH^- is the main driving force. Likewise, primary and tertiary amines such as ethylamine and 2-(dimethylamino)ethanol have been successfully employed to exfoliate protonated layered oxides. However, the extent of osmotic swelling and degree of exfoliation are strongly dependent on factors such as layer charge density, size and polarity of the swelling agent, and type of interlayer gallery ion (59).

In contrast to nanosheets without layer charge, charged 2D nanosheets can be conceived as colloids, gigantic polyions, or inorganic polyelectrolytes and are thus amenable to the solution and colloidal processing protocols that have been developed for organic polyelectrolytes and colloids. Three major techniques, namely flocculation (**Figure 8a**), electrostatic layer-by-layer (LbL) assembly (**Figure 8b**), and Langmuir–Blodgett (LB) transfer (**Figure 8c**), can be used to assemble 2D polyelectrolytes into lamellar heterostructures with varying degrees of control.

3.3.1. Flocculation. The simplest method to achieve heterolayering of different types of nanosheets is by destabilizing the colloidal suspension of one nanosheet component by the addition or in the presence of the second component. In general, flocculation can be achieved by mixing the suspensions of cationically and anionically charged nanosheets or by destabilizing a mixed suspension of different types of anionic (or cationic) nanosheets by adding an electrolyte such as NaCl (**Figure 8a**). Although flocculation is fast and simple and gives rise to bulk amounts of heterostructures (60), the control over the layer structure, layer registry, and interfacial quality is minimal. Therefore, flocculation typically gives rise to turbostratically disordered lamellar materials that are notoriously difficult to analyze. The stability of a colloidal system is largely dependent on the colloid’s surface potential, on the type and ionic strength of the electrolyte, and on the Hamaker constant (61). Dispersions of oppositely charged nanosheets are thermodynamically unstable, and nanosheet assembly is typically a fast, irreversible process whose kinetics are determined by the frequency of colloid collision and by the probability of cohesion during collision (61, 62). However, the level of actual interstratification and stacking disorder in binary solids of coflocculated nanosheets has rarely been analyzed in depth, although it may be strongly dependent on the types

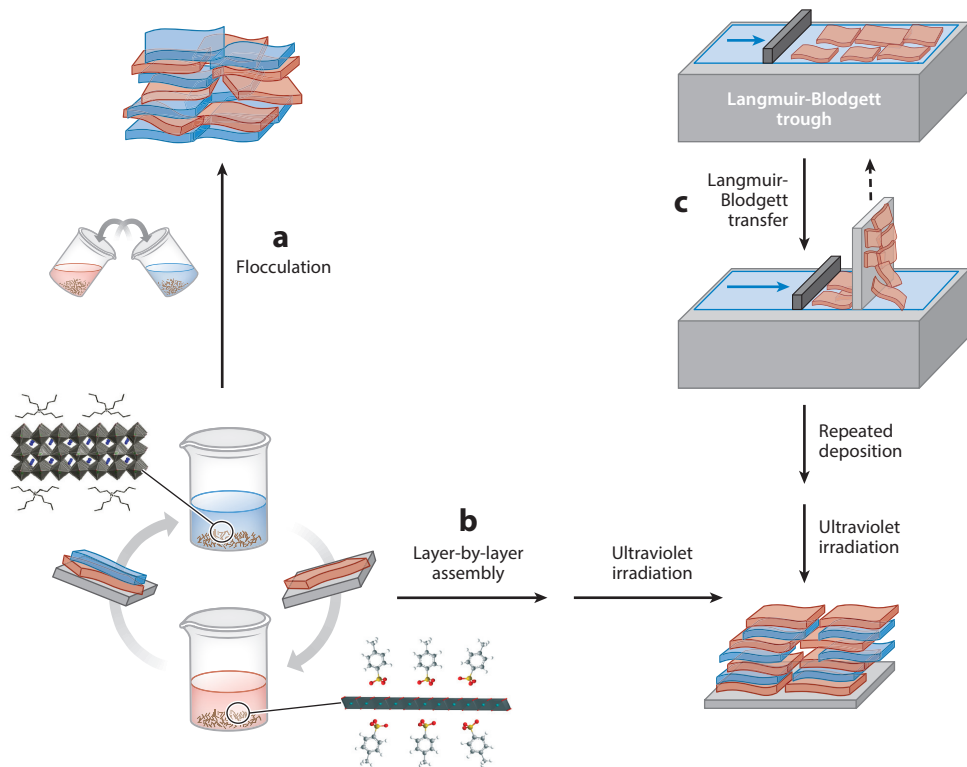


Figure 8

Schematic illustration of three wet-chemical assembly schemes for heterostructures composed of ionic (*a–c*) and/or nonionic (*c*) nanosheet building blocks: (*a*) flocculation, (*b*) electrostatic layer-by-layer assembly, and (*c*) Langmuir-Blodgett transfer.

of nanosheets, on their initial state of dispersion, and on their respective surface and interaction energies. By simulation of the diffuse scattering intensity of the resulting XRD patterns, Sasaki and coworkers showed that restacked binary colloidal suspensions of negatively charged nanosheets flocculated by KCl addition can form various types of composites ranging from fully interstratified solid solutions via costacked systems with miscibility gaps to completely phase-separated systems (63). A range of heterolayered composites have been obtained by flocculation. Owing to a notable lack of cationically charged nanosheets, most systems rely on layered double hydroxides (LDH) represented by $[M^{2+}_{1-x}M^{3+}_x(OH)_2]^{x+}[A^{n-}_{x/n}]^{x-} \cdot mH_2O$ ($M^{2+} = Mg^{2+}, Fe^{2+}, Co^{2+}, Ni^{2+}, Zn^{2+}, Cu^{2+}$, etc.; $M^{3+} = Al^{3+}, Cr^{3+}, Fe^{3+}, Co^{3+}$, etc.; $A = CO_3^{2-}, NO_3^-, Cl^-$, etc.; $x = 0.2–0.33$) as the cationic component. Restacked solids composed of montmorillonite/LDH (60), perovskite/LDH [e.g., $Mg_{0.66}Al_{0.33}(OH)_2/Ca_2Nb_3O_{10}$] (64), titanate/LDH [$Ti_{1.83}O_{0.17}/Zn_{0.69}Cr_{0.31}(OH)_2$] (65), or $Ni_{0.66}Al_{0.33}(OH)_2/TaS_2$ have been reported; the last shows the coexistence of ferromagnetism (inherent in the LDH) and superconductivity (due to TaS_2) at $T < 4$ K (66).

3.3.2. Electrostatic layer-by-layer assembly. The electrostatic LbL assembly method was introduced by Iler (67) in the late 1960s and was developed by Decher and others (68, 69) into a versatile tool to sequentially adsorb molecularly thin layers of organic polyelectrolytes and charged colloids on various substrates to create complex heterostructures by chemical design. The resulting

polyelectrolyte multilayers are composed of alternately arranged cationic and anionic polymers engineered into functional arrays used as smart coatings with tailor-made optical, mechanical, and chemical properties (69, 70). In LbL assembly, a substrate is alternately immersed into the suspensions of oppositely charged colloids at ambient temperature or slightly above, with extensive washing steps in between to remove excess (i.e., nonelectrostatically adsorbed) material (**Figure 8b**). Coverage of the substrate with a densely tiled monolayer of nanosheets is key and is sometimes achieved by priming the substrate with an organic polyelectrolyte carrying opposite charge and by the subtle control of solution pH to reduce repulsive forces between the nanosheet edges (71). The LbL process is a self-limiting process, as polyelectrolyte adsorption stops after the exposed surface charge is reversed through adsorption of a charge-compensating monolayer of the oppositely charged species. As LbL assembly is restricted to charged colloids, cationic polyelectrolytes have been used as electrostatic glue to assemble different types of anionically charged nanosheets. Examples include zirconium phosphate-layered oxide semiconductor hybrids such as (a) α -Zr(HPO₄)/PAH/K₂Nb₆O₁₇/PAH [where PAH denotes poly(allylamine hydrochloride)] (51); (b) (Ti_{0.91}O₂/PDDA/MnO₂/PDDA)_n [where PDDA denotes poly(diallyldimethylammonium chloride)] multilayers (55); and (c) mixed-layered perovskites, for example, quarternary (HCa₂Nb₃O₁₀/PDDA/HLaNb₂O₇/PDDA/HSr₂Nb₃O₁₀/PDDA/HLaNb₂O₇)_n multilayers interleaved with the pH-independent polyelectrolyte PDDA (71, 72). The last is an intriguing example of an ordered intergrowth of Dion-Jacobson (DJ)-type perovskites with perovskite block sizes of $n = 2$ and $n = 3$ and ordered A-site cations (A = La, Ca, Sr), which are not accessible by bulk synthesis (71). This bottom-up synthetic scheme opens prospects of converting artificially stacked DJ or Ruddlesden-Popper 2D perovskites into artificial 3D perovskites with an unusual distribution or order of the A-site cations by topochemical dehydration or reduction with a concomitant loss of oxygen (71–74). The presence of cationic polyelectrolytes may lead not only to increased film roughness, but also to carbonaceous residues causing interface contamination. However, controlled thermal decomposition or UV irradiation of photocatalytically active nanosheets can lead to the degradation of the organic components into charge-compensating protons or NH₄⁺ cations while leaving the inorganic multilayer components largely intact (3, 72, 75). LDH have been used as charge-compensating species in all-nanosheet-multilayer stacks as, for example, in [Mg_{0.66}Al_{0.33}(OH)₂/Ti_{0.91}O₂]_n and [Mg_{0.66}Al_{0.33}(OH)₂/Ca₂Nb₃O₁₀]_n, with $n \leq 10$ (64), or in [Eu(OH)_{3-x}/Ti_{0.91}O₂]_n multilayers showing strongly modified photoluminescence of the Eu³⁺ ions when in close proximity to the titanate layers (76). Although the LbL process allows for a high level of control regarding the strictly alternating placement of nanosheets on a substrate, the in situ monitoring of the assembly process and the atomically resolved analysis of the obtained multilayer structures are key requirements. Monitoring the UV-vis absorbance after each deposition step has proven to be a powerful tool to study the stepwise adsorption of nanosheets with characteristic optical signatures (55, 64). Likewise, spectroscopic ellipsometry (51, 71, 72) and quartz crystal microbalance techniques sensitively probe monolayer adsorption, albeit with less chemical specificity. Structural insights into the multilayer assemblies are furnished by XRD analysis of the film samples, although in most systems only out-of-plane structural information has been obtained by measurements in reflection geometry. Nevertheless, details about the lattice periodicity, number of bilayers, and disorder may be retrieved from inspection of the sharpness, profile, and number of the Bragg reflections pertaining to the basal series of reflections, the intensity of which is given by the following equation (77, 78):

$$I(00l) = \frac{1}{N} \frac{1 + \cos^2 2\theta}{\sin^2 \theta \cos \theta} F^2(00l) \frac{\sin^2(\pi Nk)}{\sin^2(\pi k)}. \quad 1.$$

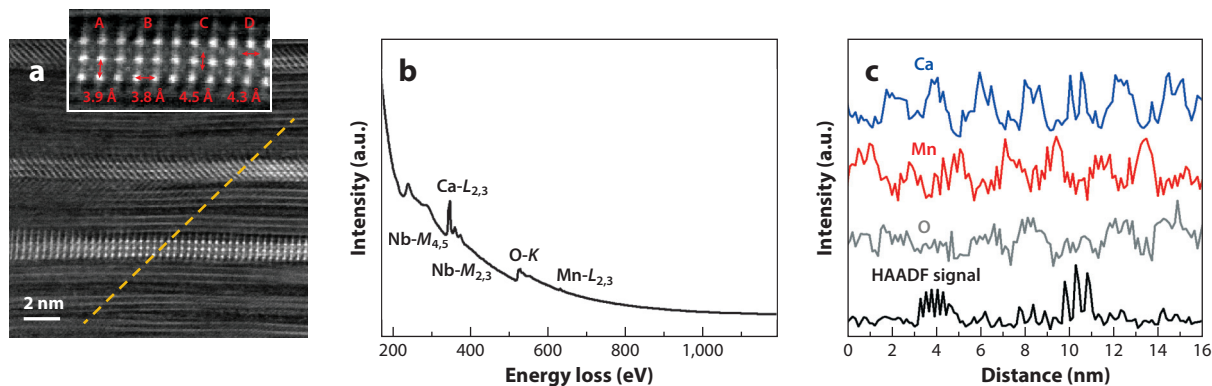


Figure 9

(a) STEM cross-sectional image of a (Mn-Al-LDH/perovskite)₁₀₀ layer-by-layer film and spatially resolved elemental analysis demonstrating successful interstratification. The inset shows the vertical (vert) and horizontal (horiz) atomic distances between (A) Nb–Nb_{horiz}, (B) Nb–Nb_{vert}, (C) Ca–Ca_{vert}, and (D) Ca–Ca_{horiz} (in red). (b) EEL sum spectra of the region shown in panel a. (c) Extracted intensity profiles of the Ca–L_{2,3}, Mn–L_{2,3}, and O–K edges and the HAADF signal taken along the yellow dashed line in panel a. LDH denotes layered double hydroxide. Adapted from Reference 80 with permission.

Here, $I(00l)$ is the scattered intensity of the basal reflections for a system of N parallel nanosheets, the second term is the Lorentz polarization factor, the third term is the structure factor, and the fourth term is the Laue interference function. The peak intensity of the $(00l)$ reflections is linearly dependent on N . The structural quality of the multilayer system may be assessed in terms of the appearance of Laue satellite fringes around the basal plane reflections, which are testament to a high degree of vertical layer orientation (77, 78). In addition, a Williamson-Hall analysis of the XRD pattern according to

$$\frac{\beta \cos \theta}{\lambda} = \frac{1}{\varepsilon} + 2\eta \frac{\sin \theta}{K\lambda}, \quad 2.$$

where β is the FWHM (full-width at half-maximum), λ the wavelength used, θ the diffraction angle, ε the domain size, η the lattice strain, and K a shape factor, allows one to quantify the domain size of coherently scattering platelets along the stacking direction as well as the lattice strain, which can be <0.08%, even for solution-deposited films (77, 79).

Whereas the above methods probe ensemble properties rather than the location of individual layers in the stack, HRTEM/STEM in combination with EELS has proven to be an invaluable tool for probing the layer sequence with high resolution down to the atomic scale. As demonstrated in **Figure 9**, the Ca₂Nb₃O₁₀/Mn-Al-LDH heterostacks show high-fidelity interstratification of the layers along the assembly direction, whereas turbostratic disorder and layer bending are observed as a consequence of the LbL assembly process (80).

3.3.3. Langmuir-Blodgett assembly. The LB method is a versatile tool to assemble, compress, and transfer molecularly thin films spread at the air/water interface to arbitrary substrates with precision at the (sub)nanoscale. In recent years, the LB method has been modified so as to enable not only the transfer of monolayers composed of amphiphilic molecules, i.e., surfactants, but also the transfer of colloidal particles such as organoclays or MoS₂ with an inherent or acquired amphiphilicity (81, 82). Although in a typical LB film assembly the amphiphile is contained in a volatile organic solvent such as chloroform, which is spread on the water subphase in a LB trough, Muramatsu et al. (83) have demonstrated the interfacial assembly of monolayer lepidocrocite-type

titanate films entirely without amphiphilic additives. The rationale for this observation is the apparent hydrophobicity of $\text{Ti}_{0.91}\text{O}_2$ nanosheets, leading to spontaneous $\text{Ti}_{0.91}\text{O}_2$ segregation at the air/water interface, which can be further enhanced by adsorption of tetrabutylammonium cations to the negatively charged nanosheets. After surface pressure equilibration, the nanosheet monolayer can be transferred by either horizontal or vertical lifting of a substrate immersed in the LB trough at a constant transfer rate (**Figure 8c**). The power and versatility of this method are given by the fact that it enables the assembly of close-packed nanosheet monolayers whose packing density can be precisely adjusted by the applied surface pressure π through recording the $\pi - A$ (A = molecular area) isotherms and adjusting the colloidal concentration. In addition, the transfer of multiple layers of neutral and ionic nanosheets with the same surface charge is possible. This feature is particularly beneficial because the vast majority of nanosheets carry a negative surface charge. Nevertheless, exfoliated nanosheet suspensions contain cationic counterions, such as tetrabutylammonium, that assist in the delamination process. Adsorption of these cations to the nanosheets floating at the air/water interface tends to deteriorate the multilayer buildup process upon subsequent layer transfers to a substrate (77). Akatsuka et al. (77) demonstrated the use of UV irradiation as a means to photocatalytically degrade the organocations after each layer transfer, thus providing clean interfaces necessary for regular layer buildup. Although this process has also been successfully applied to perovskite superlattice films composed of $(\text{LaNb}_2\text{O}_7/\text{Ca}_2\text{Nb}_3\text{O}_{10})_n$ multilayers that show strong interfacial electronic coupling giving rise to ferroelectricity (84), the generality of this approach and applicability to noncatalytic nanosheets have yet to be demonstrated.

4. POTENTIAL APPLICATIONS

The applications of nanosheet heterostructures are as diverse as their components and their combinations. Major research directions currently explore (a) the miniaturization of devices based on the integration of 2D building blocks in both vertical and lateral dimensions and (b) the fabrication of hybrid materials for energy applications, including photocatalysis, battery materials, (super)capacitors, and thermoelectrics. Clearly, the requirements in terms of interfacial quality, defect level, and layer alignment are radically different for different applications, which calls for maximum flexibility in the types of assembly processes to be employed. In this section, only selected properties of vertical heterostructures and potential applications are highlighted. A more comprehensive treatment of this topic can be found in, for example, Reference 22.

4.1. Miniaturized Electronic and Optoelectronic Devices

The ability to vertically assemble 2D layers is an important stepping stone for the realization of miniaturized, flexible/stretchable electronic and optical devices with a high density of functional components in both vertical and lateral dimensions. The integration of various 2D materials is key to obtaining complex (opto)electronic circuits with variable design in the vertical direction, opening the door to high-speed, low-power dissipation devices operating at the ultimate size-scaling limit.

4.1.1. Transistors. New field-effect transistor (FET) geometries based on integrated 2D architectures were recently developed to overcome the inherent limitations set by graphene's lack of a transport gap and the resulting low ON-OFF current ratios in graphene-based FETs. Britnell et al. (85) demonstrated a prototype field-effect tunneling transistor (FETT) consisting of vertically stacked graphene layers sandwiching an ultrathin h-BN or MoS_2 layer that acts as a vertical tunneling barrier with tunable effective height. The devices showed bipolar characteristics, where the carrier type is determined by the gate-modulated graphene, and delivered room-temperature

switching ratios of ≈ 50 and $\approx 10,000$, respectively (85, 86). Although this device architecture could be interesting for ultrafast analog electronics, the obtained current densities were typically low (86). Significant improvements in device characteristics have been made by replacing the insulating barrier (h-BN) with WS_2 in a FETT geometry (87) or by replacing the tunneling barrier with a medium-thick (36-nm), semiconducting MoS_2 channel with an ohmic metal top contact in a vertical FET (VFET) geometry (86). In the former, current modulation in excess of 1×10^6 at room temperature and high ON state currents are achieved by a combination of tunneling (at low temperatures) and thermionic electron transport in the high-temperature regime. The n -channel MoS_2 VFET device simultaneously supports high current densities (of up to $5,000 \text{ A cm}^{-2}$) and room-temperature ON-OFF current ratios of $> 10^3$ (86). A yet higher level of complexity was realized by vertically integrating a second transistor based on a p -type cobaltite [$\text{Bi}_2\text{Sr}_2\text{Co}_2\text{O}_8$ (BSCO)] with an n -channel MoS_2 VFET, thus demonstrating a complementary inverter with a larger-than-unity voltage gain and excellent switchability of the top MoS_2 VFET through the ultrathin BSCO bottom stack (86).

4.1.2. Memory devices. Vertical graphene/ MoS_2 heterostructures have also been explored as the basis for nonvolatile memory devices, which are key components for future miniaturization of flash memory technology (88). Kis and coworkers (89) developed a memory cell based on a floating gate transistor structure. In this structure, bottom graphene stripes act as source and drain contacts, MoS_2 as the semiconducting channel, and MLG as the floating gate, separated by a 6-nm HfO_2 barrier from the underlying monolayer MoS_2 and contacted by a control gate electrode. The observed hysteresis (memory window $\Delta V = 8 \text{ V}$) in the transfer characteristics of the device is testament to efficient and sustained charge trapping in the MLG layer by electron tunneling from the semiconducting channel through the oxide barrier at positive control gate voltage (program state), which can be reversed in the erase state and switched reversibly by voltage pulses (89). Different device architectures were presented by Choi et al. (90), who used h-BN as the tunneling barrier while using either graphene or MoS_2 as the conducting channel or charge-trapping layer, and vice versa, resulting in devices with large memory windows, tunable charge-trapping characteristics and ON-OFF current ratios depending on the device architecture and thickness of the individual components.

4.1.3. Optoelectronic devices. The transition from indirect-band-gap to direct-band-gap semiconducting behavior in MoS_2 and WS_2 and their strong optical absorbance ($> 10^7 \text{ m}^{-1}$ across the visible) (91) make TMDs interesting candidates for optoelectronic applications, including photodetectors, photodiodes, light-emitting devices, and photovoltaic cells. The localized character of the electronic bands, due to the strong involvement of transition metal d -orbitals in TMDs, leads to Van Hove singularities in the density of states, which result in enhanced photoabsorption in the visible range (91). An illuminated h-BN/graphene/TMD/graphene/h-BN architecture (TMD = MoS_2 , WS_2 , WSe_2) with TMD thicknesses between 5 and 50 nm revealed high photocurrents upon separation of the photogenerated electron-hole pairs by a built-in electric field across the TMD (by p -doping of the top graphene layer or by gating). MoS_2 -based devices that were modified with plasmonic Au nanoparticles showed external quantum efficiencies in excess of 30%. Similar graphene/ MoS_2 /graphene and graphene/ MoS_2 /metal stacks with a MoS_2 thickness of $\approx 50 \text{ nm}$ were exploited for gate-tunable photocurrent generation and photodetection, showing external quantum efficiencies of up to 55% and a photoresponsivity of $\approx 0.22 \text{ A W}^{-1}$ (92). An external field applied parallel to the current direction can modulate the amplitude and polarity of the photocurrent generated in dual-gated graphene/ MoS_2 /graphene heterostructures through the field effect.

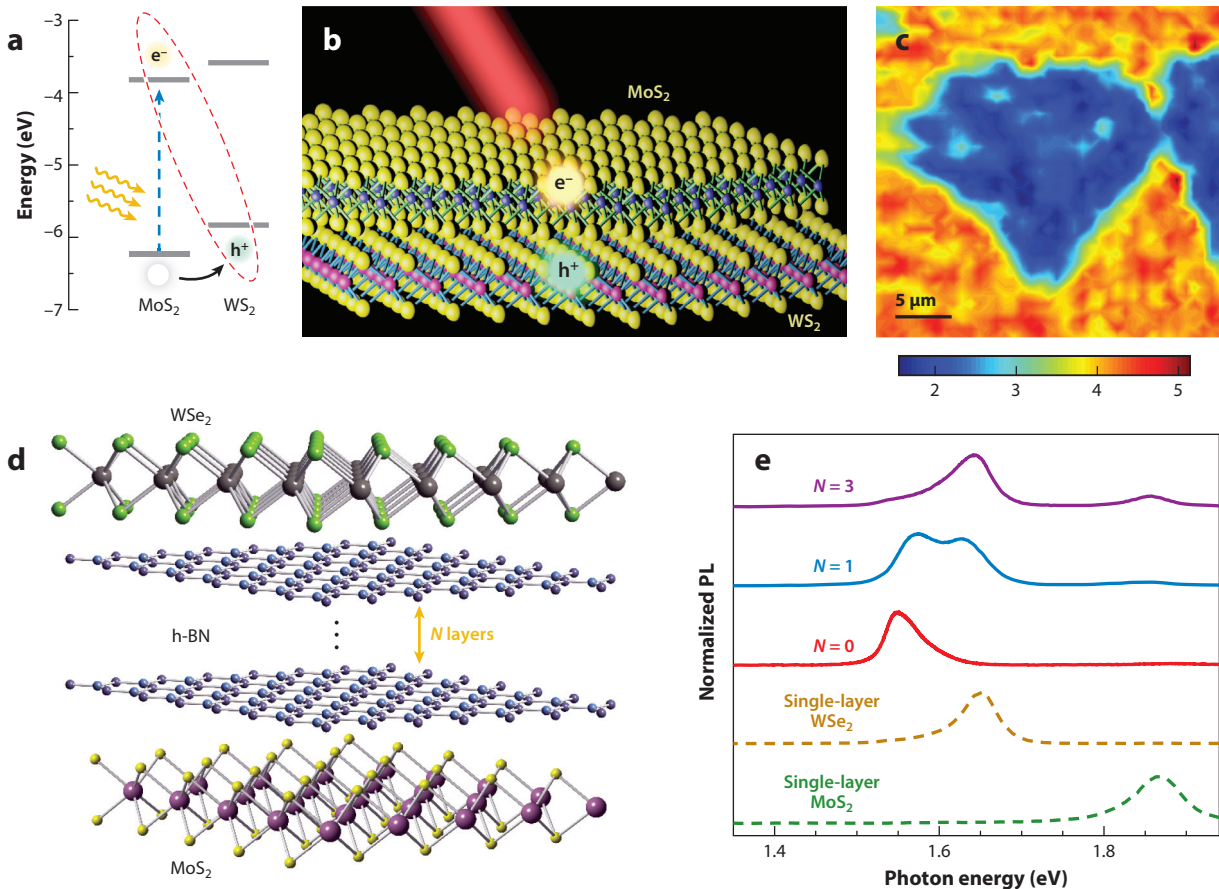


Figure 10

(a,b) Band alignment (a) and atomistic structure (b) of a type II MoS₂/WS₂ heterostructure. Electrons (e⁻) and holes (h⁺) segregate into different layers upon photoexcitation. (c) PL intensity at the MoS₂ A-exciton resonance (1.93 eV), which is quenched across the heterostructure (blue area). (d) Atomistic illustration of a WSe₂/MoS₂ bilayer separated by N h-BN layers. (e) Normalized PL spectra of the heterobilayer with N h-BN layers (N = 0, 1, and 3), single-layer WSe₂, and single-layer MoS₂. Abbreviations: h-BN, hexagonal boron nitride; PL, photoluminescence. Panels a–c adapted with permission from Reference 94. Panels d and e adapted with permission from Reference 28.

Another way of separating photogenerated electron-hole pairs in single-layer TMDs is the combination of two different TMDs to form a type II heterostructure with a band offset that assists in the transfer of electrons/holes into the conduction/valence band of the adjacent layer. In spite of the strong exciton binding energies in TMD monolayers (93), ultrafast hole transfer (<50 fs) from MoS₂ into WS₂ in photoexcited MoS₂/WS₂ heterobilayers was observed by transient absorption measurements, indicating that strong electronic coupling exists even in weakly van der Waals-bonded heterostructures (Figure 10a–c) (94). Notably, the interlayer coupling strength can be tuned by inserting insulating h-BN monolayers into MoS₂/WSe₂ heterostructures, resulting in a significant decoupling of the layers as detected by a decrease in the intensity of radiative recombination of spatially indirect excitons across the heterointerface (Figure 10d,e) (28).

4.2. Photocatalysis

As for photovoltaics, a key requirement in the design of photocatalytic systems is the efficient separation of photogenerated charge carriers to prevent recombination and enable extraction of electrons and holes for subsequent chemical conversions, such as the formation of hydrogen and oxygen from water. Bulk hybrid heterostructures composed of two types of semiconductor nanosheets have been explored as artificial heterojunctions with ultrahigh surface-to-volume ratios and large internal donor/acceptor interfaces that facilitate charge percolation to the surface and separation across the interface. This principle has been implemented by the synthesis of lamellar flocculates composed of Zn-Cr-LDH and lepidocrocite-type titanate, showing visible light-driven oxygen evolution with an activity of $\sim 1.18 \text{ mmol h}^{-1} \text{ g}^{-1}$, which is doubled compared with that of the pristine LDH (65). The observed activity was interpreted in terms of strong electronic coupling between the nanosheets resulting in efficient charge transfer from the LDH to the titanate, supported by strongly reduced photoluminescence intensity in the hybrid, as well as high levels of ordered mesoporosity and sustained stability of the nanohybrid under operation conditions. Other interstratified hybrid materials that have been tested for photocatalytic dye degradation (95), water splitting, and CO_2 conversion include various combinations of titanates with graphene oxide or graphene, where graphene acts as an electron sink that spatially separates the photogenerated electrons from the titanate (75, 96).

4.3. Capacitors

Electrochemical capacitors are promising candidates for energy storage devices owing to their high specific power and long cycle life, and efforts are being made to develop in-plane or ultrathin all-solid-state supercapacitors (97), which are intriguing energy storage components for flexible/stretchable and portable electronic devices with high safety requirements. To improve the specific capacitance of carbonaceous electrochemical double-layer capacitors that store energy by means of reversible electroadsorption of ions in the Helmholtz double layer at the electrode/electrolyte interface, graphene-based supercaps have been hybridized with pseudocapacitive nanosheets, including transition metal oxides, hydroxides, and chalcogenides. These redox-active nanosheets introduce significant faradaic capacitance (theoretically $\sim 1,370 \text{ F g}^{-1}$ for $\delta\text{-MnO}_2$ and $1,358 \text{ F g}^{-1}$ for RuO_2) through reversible redox reactions occurring at their surface (98), yielding pseudocapacitors with greatly enhanced energy density even at moderate mass loading with electroactive nanosheets (99, 100). To achieve maximum performance of hybrid supercapacitors, high intrinsic conductivity, maximized surface area, controllable pore topologies, and fast, reversible faradaic processes at the surface of the redox-active nanosheets are important attributes, some of which are inherent in the loosely stacked, lamellar 2D topology. The combination of graphene or (reduced) graphene oxide [(R)GO] and transition metal oxide-based nanosheets by in situ solvothermal synthesis or flocculation has been a successful strategy to obtain hybrid materials that show high capacitance, rate performance, and cycling life. A large number of $\delta\text{-MnO}_2$ /graphene hybrids have been synthesized, notably ultrathin in-plane supercapacitor geometries obtained by a vacuum filtration process with a specific capacitance of $>200 \text{ F g}^{-1}$ at high scan rates of 400 mV s^{-1} (99). Other examples include Co-Al-LDH/GO hybrids with specific capacitances of up to $1,031 \text{ F g}^{-1}$ (101), $\text{Mn}_3(\text{PO}_4)_2 \cdot 3\text{H}_2\text{O}$ /graphene hybrids with a specific capacitance of $2,086 \text{ F g}^{-1}$ at 1 mV s^{-1} (102), and even MoS_2 /RGO composites exhibiting a specific capacitance of up to 265 F g^{-1} at 10 mV s^{-1} , depending on the MoS_2 loading (100).

Pushing miniaturization to its limit, Wang et al. (97) recently fabricated an ultrathin parallel-plate-type ceramic capacitor based on $\text{Ru}_{0.95}\text{O}_2^{0.2-}$ (metal)/ $\text{Ca}_2\text{Nb}_3\text{O}_{10}^-$ (insulator)/ $\text{Ru}_{0.95}\text{O}_2^{0.2-}$

(metal) LB multilayer structures with a total thickness of less than 30 nm. Electrical measurements gave a capacitance density of $\sim 27.5 \mu\text{F cm}^{-1}$, which is far superior to state-of-the-art HfO_2 -based and commercial capacitor devices, thus boding well for the design of miniaturized all-nanosheet high- κ MIM (metal-insulator-metal) devices through solution processing.

4.4. Ultrathin Sensing Devices

Miniaturized sensing devices based on vertical heterostructures offer huge potential in medical diagnostics and environmental monitoring owing to their high surface-to-volume ratio, tunable electronic and optical properties, and ease of handling. Ultrasensitive detection of specific DNA or peptide sequences was recently demonstrated by utilizing probe DNAs immobilized on the surface of graphene-on- MoS_2 heterostructures (**Figure 11**). Complementary target DNA can be detected with a high selectivity down to attomolar (10^{-18} M) concentrations by monitoring the increase in TMD photoluminescence intensity, which is enhanced by lowering the electron concentration in MoS_2 upon DNA hybridization in the presence of the graphene top layer (103).

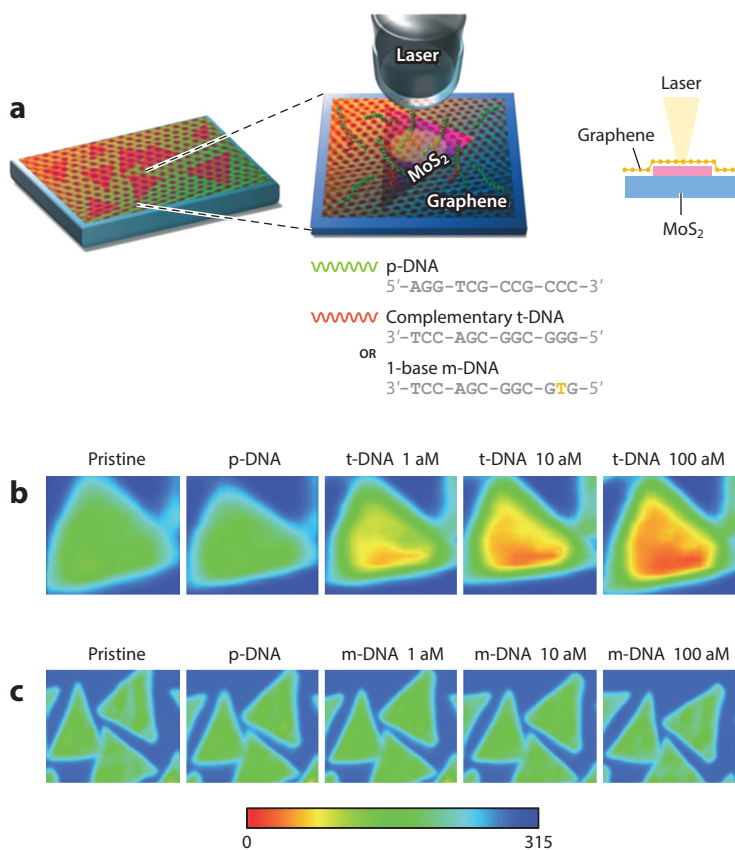


Figure 11

(a) Illustration of the label-free DNA detection process based on a graphene/ MoS_2 sensor. (b,c) Lateral PL mappings of the heterostructure hybridized with (b) complementary t-DNA and (c) one-base m-DNA. The DNA concentration is given at the tops of the PL maps. Abbreviations: m-DNA, mismatched DNA; p-DNA, probe DNA; PL, photoluminescence; t-DNA, target DNA. Adapted with permission from Reference 103.

5. CONCLUSIONS AND OUTLOOK

Nanoarchitectonics, most prominently represented by the emerging field of 2D heterostructures, has been refueled by the advent of graphene nanoscience and is likely to thrive and mature as the availability of 2D building blocks is diversified further and the tools for making precise heterostructures are optimized. In fact, most of the van der Waals heterostructures presented to date are examples of unique handicraft and elaborate nanofabrication rather than the result of automated large-scale assembly. Yet for heterostructures to transition from the realm of fundamental research to real-world applications, fabrication protocols need to be developed that allow for a more flexible, automated, and scalable design of heterostructures and that are amenable to integration into existing microfabrication schemes.

Whereas the mechanical transfer of neutral 2D nanosheets gives rise to atomically clean interfaces, this method is inherently limited with respect to the deposition of multilayer heterostructures with bulk dimensions. Although potentially powerful, CVD methods still suffer from the inability to strictly deposit monolayers of various materials with large lateral dimensions onto arbitrary surfaces. In contrast, the assembly of nanosheets by solution-assisted methods is inexpensive; is instrumentally simple; and at the same time furnishes a wide range of heterostructures with bulk dimensions, albeit at the expense of interfacial quality.

Further research into the large-scale assembly of 2D heterostructures is certainly warranted by the impressive scope of new physical phenomena and unique properties already discovered or expected to arise from the judicious combination of insulating, semiconducting, or metallic nanosheets with a unique level of control. Both the ability to sculpture artificial solids with engineered properties—a bottom-up version of the materials genome—and the prospect of ultimate device miniaturization based on 2D heterostructures are hallmarks that will define and drive the progress in this emerging field.

DISCLOSURE STATEMENT

The author is not aware of any affiliations, memberships, funding, or financial holdings that might be perceived as affecting the objectivity of this review.

ACKNOWLEDGMENTS

Financial support from the Max Planck Society, LMU, Cluster of Excellence Nanosystems Initiative Munich (NIM), Center for Nanoscience, Deutsche Forschungsgemeinschaft (DFG), and Fonds der Chemischen Industrie (FCI) is gratefully acknowledged. I wish to express my gratitude to Pirmin Ganter, Claudia Kamella, Daniel Weber, and Christian Ziegler for their help in preparing this article and figures.

LITERATURE CITED

1. Geim AK, Grigorieva IV. 2013. Van der Waals heterostructures. *Nature* 499:419–25
2. Ponomarenko LA, Geim AK, Zhukov AA, Jalil R, Morozov SV, et al. 2011. Tunable metal-insulator transition in double-layer graphene heterostructures. *Nat. Phys.* 7:958–61
3. Osada M, Sasaki T. 2012. Two-dimensional dielectric nanosheets: novel nanoelectronics from nanocrystal building blocks. *Adv. Mater.* 24:210–28
4. Butler SZ, Hollen SM, Cao L, Cui Y, Gupta JA, et al. 2013. Progress, challenges, and opportunities in two-dimensional materials beyond graphene. *ACS Nano* 7:2898–926
5. Schlom DG, Chen L-Q, Pan X, Schmehl A, Zurbuchen MA. 2008. A thin film approach to engineering functionality into oxides. *J. Am. Ceram. Soc.* 91:2429–54

6. Azadmanjiri J, Berndt CC, Wang J, Kapoor A, Srivastava VK, Wen C. 2014. A review on hybrid nanolaminate materials synthesized by deposition techniques for energy storage applications. *J. Mater. Chem. A* 2:3695–708
7. Rouxel J, Meerschaut A, Wiegiers GA. 1995. Chalcogenide misfit layer compounds. *J. Alloys Compd.* 229:144–57
8. Westover RD, Atkins RA, Ditto JJ, Johnson DC. 2014. Synthesis of $[(\text{SnSe})_{1.15}]_m(\text{TaSe}_2)_n$ ferecrystals: structurally tunable metallic compounds. *Chem. Mater.* 26:3443–49
9. Bianco E, Butler S, Jiang S, Restrepo OD, Windl W, Goldberger JE. 2013. Stability and exfoliation of germanane: a germanium graphane analogue. *ACS Nano* 7:4414–21
10. Jiang S, Butler S, Bianco E, Restrepo OD, Windl W, Goldberger JE. 2014. Improving the stability and optical properties of germanane via one-step covalent methyl-termination. *Nat. Commun.* 5:3389
11. Naguib M, Kurtoglu M, Presser V, Lu J, Niu J, et al. 2011. Two-dimensional nanocrystals produced by exfoliation of Ti_3AlC_2 . *Adv. Mater.* 23:4248–53
12. Schwinghammer K, Mesch MB, Duppel V, Ziegler C, Senker J, Lotsch BV. 2014. Crystalline carbon nitride nanosheets for improved visible-light hydrogen evolution. *J. Am. Chem. Soc.* 136:1730–33
13. Algara-Siller G, Severin N, Chong SY, Björkman T, Palgrave RG, et al. 2014. Triazine-based graphitic carbon nitride: a two-dimensional semiconductor. *Angew. Chem.* 53:7450–55
14. Kory MJ, Wörle M, Weber T, Payamyar P, van de Poll SW, et al. 2014. Gram-scale synthesis of two-dimensional polymer crystals and their structure analysis by X-ray diffraction. *Nat. Chem.* 6:779–84
15. Rodenas T, Luz I, Prieto G, Seoane B, Miro H, et al. 2015. Metal–organic framework nanosheets in polymer composite materials for gas separation. *Nat. Mater.* 14:48–55
16. Rao CNR, Matte HSSR, Maitra U. 2013. Graphene analogues of inorganic layered materials. *Angew. Chem. Int. Ed.* 52:13162–85
17. Wang QH, Kalantar-Zadeh K, Kis A, Coleman JN, Strano MS. 2012. Electronics and optoelectronics of two-dimensional transition metal dichalcogenides. *Nat. Nanotechnol.* 7:699–712
18. Balendhran S, Walia S, Nili H, Ou JZ, Zhuiykov S, et al. 2013. Two-dimensional molybdenum trioxide and dichalcogenides. *Adv. Funct. Mater.* 23:3952–70
19. Rao CNR, Maitra U. 2015. Inorganic graphene analogs. *Annu. Rev. Mater. Res.* 45:29–62
20. Ma R, Sasaki T. 2015. Organization of artificial superlattices utilizing nanosheets as a building block and exploration of their advanced functions. *Annu. Rev. Mater. Res.* 45:111–27
21. Caldwell JD, Anderson TJ, Culbertson JC, Jernigan GG, Hobart KD, et al. 2010. Technique for the dry transfer of epitaxial graphene onto arbitrary substrates. *ACS Nano* 4:1108–14
22. Lim H, Yoon SI, Kim G, Jang A-R, Shin SH. 2014. Stacking of two-dimensional materials in lateral and vertical directions. *Chem. Mater.* 26:4891–903
23. Schneider GF, Calado VE, Zandbergen H, Vandersypen LMK, Dekker C. 2010. Wedging transfer of nanostructures. *Nano Lett.* 10:1912–16
24. Li H, Wu J, Huang X, Yin Z, Liu J, Zhang H. 2014. A universal, rapid method for clean transfer of nanostructures onto various substrates. *ACS Nano* 8:6563–70
25. Song J, Kam F-Y, Png R-Q, Seah W-L, Zhuo J-M, et al. 2013. A general method for transferring graphene onto soft surfaces. *Nat. Nanotechnol.* 8:356–62
26. Wang L, Meric I, Huang PY, Gao Q, Gao Y, et al. 2013. One-dimensional electrical contact to a two-dimensional material. *Science* 342:614–17
27. Woods CR, Britnell L, Eckmann A, Ma RS, Lu JC, et al. 2014. Commensurate–incommensurate transition in graphene on hexagonal boron nitride. *Nat. Phys.* 10:451–56
28. Fang H, Battaglia C, Carraro C, Nemsak S, Ozdol B, et al. 2014. Strong interlayer coupling in van der Waals heterostructures built from single-layer chalcogenides. *PNAS* 111:6198–202
29. Haigh SJ, Gholinia A, Jalil R, Romani S, Britnell L, et al. 2012. Cross-sectional imaging of individual layers and buried interfaces of graphene-based heterostructures and superlattices. *Nat. Mater.* 11:764–67
30. Koma A, Sunouchi K, Miyajima T. 1984. Fabrication and characterization of heterostructures with subnanometer thickness. *Microelectron. Eng.* 2:129–36
31. Koma A, Sunouchi K, Miyajima T. 1985. Electronic structure of a monolayer NbSe_2 film grown heteroepitaxially on the cleaved face of 2H-MoS_2 . In *Proc. 17th Int. Conf. Phys. Semicond.*, pp. 1465–68. New York: Springer

32. Koma A. 1999. Van der Waals epitaxy for highly lattice-mismatched systems. *J. Cryst. Growth* 201–202:236–41
33. Rümmele H, Bachmatiuk A, Scott A, Börrnert F, Warner JH, et al. 2010. Direct low-temperature nanographene CVD synthesis over a dielectric insulator. *ACS Nano* 4:4206–10
34. Ji Q, Zhang Y, Gao T, Zhang Y, Ma D, et al. 2013. Epitaxial monolayer MoS₂ on mica with novel photoluminescence. *Nano Lett.* 13:3870–77
35. Tang S, Wang H, Zhang Y, Li A, Xie H, et al. 2013. Precisely aligned graphene grown on hexagonal boron nitride by catalyst free chemical vapor deposition. *Sci. Rep.* 3:2666
36. Yang W, Chen G, Shi Z, Liu C-C, Zhang L, et al. 2013. Epitaxial growth of single-domain graphene on hexagonal boron nitride. *Nat. Mater.* 12:792–97
37. Shi Y, Li H, Li L-J. 2015. Recent advances in controlled synthesis of two-dimensional transition metal dichalcogenides via vapour deposition techniques. *Chem. Soc. Rev.* In press; doi: 10.1039/C4CS00256C
38. Kim J, Bayram C, Park H, Cheng C-W, Dimitrakopoulos C, et al. 2014. Principle of direct van der Waals epitaxy of single-crystalline films on epitaxial graphene. *Nat. Commun.* 5:4836
39. Zhan Y, Liu Z, Najmaei S, Ajayan PM, Lou J. 2012. Large-area vapor-phase growth and characterization of MoS₂ atomic layers on a SiO₂ substrate. *Small* 8:966–71
40. Song J-G, Park J, Lee W, Choi T, Jung H, et al. 2013. Layer-controlled, wafer-scale, and conformal synthesis of tungsten disulfide nanosheets using atomic layer deposition. *ACS Nano* 7:11333–40
41. Lee Y-H, Zhang X-Q, Zhang W, Chang M-T, Lin C-T, et al. 2012. Synthesis of large-area MoS₂ atomic layers with chemical vapor deposition. *Adv. Mater.* 24:2320–25
42. Lee Y-H, Yu L, Wang H, Fang W, Ling X, et al. 2013. Synthesis and transfer of single-layer transition metal disulfides on diverse surfaces. *Nano Lett.* 13:1852–57
43. Wu S, Huang C, Aivazian G, Ross JS, Cobden DH, Xu X. 2013. Vapor–solid growth of high optical quality MoS₂ monolayers with near-unity valley polarization. *ACS Nano* 7:2768–72
44. Shi Y, Zhou W, Lu A-Y, Fang W, Lee Y-H, et al. 2012. Van der Waals epitaxy of MoS₂ layers using graphene as growth templates. *Nano Lett.* 12:2784–91
45. Saidi WA. 2014. Van der Waals epitaxial growth of transition metal dichalcogenides on pristine and N-doped graphene. *Cryst. Growth Des.* 14:4920–28
46. Shim GW, Yoo K, Seo S-B, Shin J, Jung DY, et al. 2010. Large-area single-layer MoSe₂ and its van der Waals heterostructures. *ACS Nano* 8:6655–62
47. Lin Y-C, Lu N, Perea-Lopez N, Li J, Lin Z, et al. 2014. Direct synthesis of van der Waals solids. *ACS Nano* 8:3715–23
48. Ling X, Lee Y-H, Lin Y, Fang WJ, Yu L, et al. 2014. Role of the seeding promoter in MoS₂ growth by chemical vapor deposition. *Nano Lett.* 14:464–72
49. Bauer E, van der Merwe JH. 1986. Structure and growth of crystalline superlattices: from monolayer to superlattice. *Phys. Rev. B* 33:3657–71
50. Noh M, Johnson CD, Hornbostel MD, Thiel J, Johnson DC. 1996. Control of reaction pathway and the nanostructure of final products through the design of modulated elemental reactants. *Chem. Mater.* 8:1625–35
51. Keller SW, Kim H-N, Mallouk TE. 1994. Layer-by-layer assembly of intercalation compounds and heterostructures on surfaces: toward molecular “beaker” epitaxy. *J. Am. Chem. Soc.* 116:8817–18
52. Decher G, Hong J-D. 1991. Buildup of ultrathin multilayer films by a self-assembly process, I consecutive adsorption of anionic and cationic bipolar amphiphiles. *Makromol. Chem. Macromol. Symp.* 46:321–27
53. Buck MR, Schaak RE. 2013. Emerging strategies for the total synthesis of inorganic nanostructures. *Angew. Chem. Int. Ed.* 52:6154–78
54. Huang J, Ma R, Ebina Y, Fukuda K, Takada K, Sasaki T. 2010. Layer-by-layer assembly of TaO₃ nanosheet/polycation composite nanostructures: multilayer film, hollow sphere, and its photocatalytic activity for hydrogen evolution. *Chem. Mater.* 22:2582–87
55. Sakai N, Fukuda K, Omomo Y, Ebina Y, Takada K, Sasaki T. 2008. Hetero-nanostructured films of titanium and manganese oxide nanosheets: photoinduced charge transfer and electrochemical properties. *J. Phys. Chem. C* 112:5197–202
56. Li B-W, Osada M, Akatsuka K, Ebina Y, Ozawa TC, Sasaki T. 2011. Solution-based fabrication of perovskite multilayers and superlattices using nanosheet process. *Jpn. J. Appl. Phys.* 50:9S2

57. Sasaki T, Ebina Y, Tanaka T, Harada M, Watanabe M, Decher G. 2001. Layer-by-layer assembly of titania nanosheet/polycation composite films. *Chem. Mater.* 13:4661–67
58. Osada M, Ebina Y, Takada K, Sasaki T. 2006. Gigantic magneto–optical effects in multilayer assemblies of two-dimensional titania nanosheets. *Adv. Mater.* 18:295–99
59. Geng F, Ma R, Ebina Y, Yamauchi Y, Miyamoto N, Sasaki T. 2014. Gigantic swelling of inorganic layered materials: a bridge to molecularly thin two-dimensional nanosheets. *J. Am. Chem. Soc.* 136:5491–500
60. Chalasani R, Gupta A, Vasudevan S. 2013. Engineering new layered solids from exfoliated inorganics: a periodically alternating hydroxalcite–montmorillonite layered hybrid. *Sci. Rep.* 3:3498
61. Kohler H-H, Woelki S. 2005. Surface charge and surface potential. In *Surfactant Science Series 126: Coagulation and Flocculation*, ed. B Dobias, H Stechmesser. Boca Raton, FL: CRC. 2nd ed.
62. Harper WR. 1934. On the theory of the coagulation of colloids and of smokes. *Trans. Faraday Soc.* 30:636–43
63. Onoda M, Liu Z, Ebina Y, Takada K, Sasaki T. 2011. X-ray diffraction study on restacked flocculates from binary colloidal nanosheet systems $\text{Ti}_{0.91}\text{O}_2\text{–MnO}_2$, $\text{Ca}_2\text{Nb}_3\text{O}_{10}\text{–Ti}_{0.91}\text{O}_2$, and $\text{Ca}_2\text{Nb}_3\text{O}_{10}\text{–MnO}_2$. *J. Phys. Chem. C* 115:8555–66
64. Li L, Ma R, Ebina Y, Fukuda K, Takada K, Sasaki T. 2007. Layer-by-layer assembly and spontaneous flocculation of oppositely charged oxide and hydroxide nanosheets into inorganic sandwich layered materials. *J. Am. Chem. Soc.* 129:8000–7
65. Gunjaker JL, Kim TW, Kim HN, Kim IY, Hwang S-J. 2011. Mesoporous layer-by-layer ordered nanohybrids of layered double hydroxide and layered metal oxide: highly active visible light photocatalysts with improved chemical stability. *J. Am. Chem. Soc.* 133:14998–5007
66. Coronado E, Martí-Gastaldo C, Navarro-Moratalla E, Ribera A, Blundell SJ, Baker PJ. 2010. Coexistence of superconductivity and magnetism by chemical design. *Nat. Chem.* 2:1031–36
67. Iler RK. 1966. Multilayers of colloidal particles. *J. Colloid Interface Sci.* 21:569–74
68. Fendler JH. 1996. Self-assembled nanostructured materials. *Chem. Mater.* 8:1616–24
69. Lvov Y, Decher G, Möhwald H. 1993. Assembly, structural characterization, and thermal behavior of layer-by-layer deposited ultrathin films of poly(vinyl sulfate) and poly(allylamine). *Langmuir* 9:481–86
70. Srivastava S, Kotov NA. 2008. Composite layer-by-layer (LBL) assembly with inorganic nanoparticles and nanowires. *Acc. Chem. Res.* 41:1831–41
71. Schaak RE, Mallouk TE. 2000. Self-assembly of tiled perovskite monolayer and multilayer. *Thin Films Chem. Mater.* 12:2513–16
72. Fang M, Kim CH, Saupe GB, Kim H-N, Waraksa CC, et al. 1999. Layer-by-layer growth and condensation reactions of niobate and titanoniobate thin films. *Chem. Mater.* 11:1526–32
73. Schaak RE, Mallouk TE. 2002. Perovskites by design: a toolbox of solid-state reactions. *Chem. Mater.* 14:1455–71
74. Schaak RE, Mallouk TE. 2000. Topochemical synthesis of three-dimensional perovskites from lamellar precursors. *J. Am. Chem. Soc.* 122:2798–803
75. Manga KK, Zhou Y, Yan Y, Loh KP. 2009. Multilayer hybrid films consisting of alternating graphene and titania nanosheets with ultrafast electron transfer and photoconversion properties. *Adv. Funct. Mater.* 19:3638–43
76. Ida S, Sonoda Y, Ikeue K, Matsumoto Y. 2010. Drastic changes in photoluminescence properties of multilayer films composed of europium hydroxide and titanium oxide nanosheets. *Chem. Commun.* 46:877–79
77. Akatsuka K, Haga M-A, Ebina Y, Osada M, Fukuda K, Sasaki T. 2009. Construction of highly ordered lamellar nanostructures through Langmuir–Blodgett deposition of molecularly thin titania nanosheets tens of micrometers wide and their excellent dielectric properties. *ACS Nano* 3:1097–106
78. Sasaki T, Ebina Y, Watanabe M, Decher G. 2000. Multilayer ultrathin films of molecular titania nanosheets showing highly efficient UV-light absorption. *Chem. Commun.* 2000:2163–64
79. Williamson GK, Hall WH. 1953. X-ray line broadening from filed aluminum and wolfram. *Acta Metall.* 1:22–31
80. Ziegler C, Werner S, Bugnet M, Wörsching M, Duppel V, et al. 2013. Artificial solids by design: assembly and electron microscopy study of nanosheet-derived heterostructures. *Chem. Mater.* 25:4892–900

81. Kotov NA, Meldrum FC, Fendler JH, Tombácz E, Dèkány I. 1994. Spreading of clay organocomplexes on aqueous solutions: construction of Langmuir–Blodgett clay organocomplex multilayer films. *Langmuir* 10:3797–804
82. Taguchi Y, Kimura R, Azumi R, Tachibana H, Koshizaki N, et al. 1998. Fabrication of hybrid layered films of MoS₂ and an amphiphilic ammonium cation using the Langmuir–Blodgett technique. *Langmuir* 14:6550–55
83. Muramatsu M, Akatsuka K, Ebina Y, Wang K, Sasaki T, et al. 2005. Fabrication of densely packed titania nanosheet films on solid surface by use of Langmuir–Blodgett deposition method without amphiphilic additives. *Langmuir* 21:6590–95
84. Li B-W, Osada M, Ozawa TC, Ebina Y, Akatsuka K, et al. 2010. Engineered interfaces of artificial perovskite oxide superlattices via nanosheet deposition process. *ACS Nano* 4:6673–80
85. Britnell L, Gorbachev RV, Jalil R, Belle BD, Schedin F, et al. 2012. Field-effect tunneling transistor based on vertical graphene heterostructures. *Science* 335:947–50
86. Yu WJ, Li Z, Zhou H, Chen Y, Wang Y, et al. 2013. Vertically stacked multi-heterostructures of layered materials for logic transistors and complementary inverters. *Nat. Mater.* 12:246–52
87. Georgiou T, Jalil R, Belle BD, Britnell L, Gorbachev RV, et al. 2013. Vertical field-effect transistor based on graphene–WS₂ heterostructures for flexible and transparent electronics. *Nat. Nanotechnol.* 8:100–3
88. Hong AJ, Song EB, Yu HS, Allen MJ, Kim J, et al. 2011. Graphene flash memory. *ACS Nano* 5:7812–17
89. Bertolazzi S, Krasnozhan D, Kis A. 2013. Nonvolatile memory cells based on MoS₂/graphene heterostructures. *ACS Nano* 7:3246–52
90. Choi MS, Lee G-H, Yu Y-J, Lee D-Y, Lee SH, et al. 2012. Controlled charge trapping by molybdenum disulphide and graphene in ultrathin heterostructured memory devices. *Nat. Commun.* 4:1624
91. Britnell L, Ribeiro RM, Eckmann A, Jalil R, Belle BD, et al. 2013. Strong light-matter interactions in heterostructures of atomically thin films. *Science* 340:1311–14
92. Yu WJ, Liu Y, Zhou H, Yin A, Li Z, et al. 2013. Highly efficient gate-tunable photocurrent generation in vertical heterostructures of layered materials. *Nat. Nanotechnol.* 8:952–58
93. Qiu DY, da Jornada FH, Louie SG. 2013. Optical spectrum of MoS₂: many-body effects and diversity of exciton states. *Phys. Rev. Lett.* 111:216805
94. Hong X, Kim J, Shi S-F, Zhang Y, Jin C, et al. 2014. Ultrafast charge transfer in atomically thin MoS₂/WS₂ heterostructures. *Nat. Nanotechnol.* 9:682–86
95. Lin B, Sun P, Zhou Y, Jiang S, Gao B, Chen Y. 2014. Interstratified nanohybrid assembled by alternating cationic layered double hydroxide nanosheets and anionic layered titanate nanosheets with superior photocatalytic activity. *J. Hazard. Mater.* 280:156–63
96. Tu W, Zhou Y, Liu Q, Tian Z, Gao J, et al. 2012. Robust hollow spheres consisting of alternating titania nanosheets and graphene nanosheets with high photocatalytic activity for CO₂ conversion into renewable fuels. *Adv. Funct. Mater.* 22:1215–21
97. Wang C, Osada M, Ebina Y, Li B-W, Akatsuka K, et al. 2014. All-nanosheet ultrathin capacitors assembled layer-by-layer via solution-based processes. *ACS Nano* 8:2658–66
98. Yu G, Xie X, Pan L, Bao Z, Cui Y. 2013. Hybrid nanostructured materials for high-performance electrochemical capacitors. *Nano Energy* 2:213–14
99. Peng L, Peng X, Liu B, Wu C, Xie Y, Yu G. 2013. Ultrathin two-dimensional MnO₂/graphene hybrid nanostructures for high-performance, flexible planar supercapacitors. *Nano Lett.* 13:2151–57
100. da Silveira Firmiano EG, Rabelo AC, Dalmaschio CJ, Pinheiro AN, Pereira EC, et al. 2014. Supercapacitor electrodes obtained by directly bonding 2D MoS₂ on reduced graphene oxide. *Adv. Energy Mater.* 4:1301380
101. Wang L, Wang D, Dong XY, Zhang ZJ, Pei XF, et al. 2011. Layered assembly of graphene oxide and Co–Al layered double hydroxide nanosheets as electrode materials for supercapacitors. *Chem. Commun.* 47:3556–58
102. Yang C, Dong L, Chen Z, Lu H. 2014. High-performance all-solid-state supercapacitor based on the assembly of graphene and manganese(II) phosphate nanosheets. *J. Phys. Chem. C* 118:18884–91
103. Loan PTK, Zhang W, Lin C-T, Wei K-H, Li L-J, Chen C-H. 2014. Graphene/MoS₂ heterostructures for ultrasensitive detection of DNA hybridization. *Adv. Mater.* 26:4838–44